Biophys J BioFAST, published on August 18, 2006 as doi:10.1529/biophysj.106.084806

This un-edited manuscript has been accepted for publication in Biophysical Journal and is freely available on BioFast at www.biophysj.org. The final copyedited version of the paper may be found at www.biophysj.org.

Nonmuscle Myosin IIA-dependent Force Inhibits Cell Spreading and Drives F-actin Flow

Yunfei Cai*, Nicolas Biais*, Gregory Giannone*, Monica Tanase*, Guoying Jiang*, Jake M. Hofman†, Chris H.Wiggins‡, Pascal Silberzan§, Axel Buguin§, Benoit Ladoux¶ and Michael P. Sheetz*

*Department of Biological Sciences, Columbia University, 1212 Amsterdam Ave., New York, NY 10027, USA

†Department of Physics, Columbia University, 538 W. 120th St, New York, NY 10027, USA

‡Department of Applied Physics and Applied Mathematics, Center for Computational Biology and Bioinformatics, Columbia University, 500 W 120th St, New York, NY 10027, USA

§Physico-Chimie Curie, Unité Mixte de Recherche Centre National de la Recherche Scientifique 168, Institut Curie, 26 Rue d'Ulm, F-75248 Paris, France

¶Matière et Systèmes Complexes, CNRS UMR 7057/Université Paris 7, Tour 33-34, 2 place Jussieu 75005 Paris, France

Correspondence and proofs should be sent to: Dr. Michael P. Sheetz, Dept. of Biological Sciences, Columbia University, Sherman Fairchild Center, Rm. 713, 1212 Amsterdam Ave. New York, NY 10027, USA. Tel.: 212-854-4857. Fax: 212-854-6399
Email: ms2001@columbia.edu

Running title: Myosin IIA Regulates Cell Motility

Keywords: RNA interference, fibroblast, deformable micro-post, cytoskeleton, motility, total internal reflection fluorescence microscopy

Abbreviation list

GFP	Green fluorescent protein
LPA	Lysophosphatidic acid
MEF	Mouse embryonic fibroblast
NMM	Nonmuscle myosin
RNAi	RNA interference
TIRF	Total internal reflection fluorescence

Copyright 2006 by The Biophysical Society.

ABSTRACT

Nonmuscle myosin IIA (NMM-IIA) is involved in the formation of focal adhesions and neurite retraction. However, the role of NMM-IIA in these functions remains largely unknown. Using RNA interference (RNAi) as a tool to decrease NMM-IIA expression, we have found that NMM-IIA is the major myosin involved in traction force generation and retrograde F-actin flow in mouse embryonic fibroblast (MEF) cells. Quantitative analyses revealed that ~60% of traction force on fibronectin-coated surfaces is contributed by NMM-IIA and ~30% by NMM-IIB. The retrograde F-actin flow decreased dramatically in NMM-IIA-depleted cells, but seemed unaffected by NMM-IIB deletion. In addition, we found that depletion of NMM-IIA caused cells to spread at a higher rate and to a greater area on fibronectin substrates during the early spreading period, whereas deletion of NMM-IIB appeared to have no effect on spreading. The distribution of NMM-IIA was concentrated on the dorsal surface and approached the ventral surface in the periphery whereas NMM-IIB was primarily concentrated around the nucleus and to a lesser extent at the ventral surface in cell periphery. Our results suggest that NMM-IIA is involved in generating a coherent cytoplasmic contractile force from one side of the cell to the other through the crosslinking and the contraction of dorsal actin filaments.

INTRODUCTION

Myosin IIs are actin-based motor proteins in eukaryotic cells. They form bipolar filaments and are presumed to contract the actin cytoskeleton. Lower eukaryotes such as *Dictyostelium d.* express a single myosin II protein. In contrast, higher eukaryotes express a variety of myosin IIs which are classified into muscle myosin IIs and nonmuscle myosin IIs (NMM-IIs) (1). Activities of NMM-IIs play important roles in a variety of cell functions ranging from mitotic spindle assembly (2) to cytokinesis (3), cell spreading (4-6), cell migration (7), and growth cone outgrowth (8).

Thus far, three different nonmuscle myosin II isoforms (NMM-IIA, MMM-IIB, and NMM-IIC) have been identified in higher eukaryotes and they are widely distributed in human and mouse organs but exhibit differential tissue expression patterns (9). Of them, NMM-IIC is absent during the earliest stages of development (9). Most cells in vertebrates express comparable levels of NMM-IIA and NMM-IIB (1) with some exceptions such as neuronal cells in which NMM-IIB is predominantly expressed (1,10). In both neuronal (10) and non-neuronal cells (11-15), NMM-IIA and NMM-IIB have distinct but overlapping distributions. Depending on cell types, the same NMM-II isoform may be distributed differently. Furthermore, both NMM-IIA and NMM-IIB interact with different proteins (16-19), which indicates that they may have distinct functions. Finally, NMM-IIA and NMM-IIB undergo dynamic reorganization in motile cells (13,15,20), implying that their biological functions are related to their dynamic reorganization.

Deletion of NMM-IIB results in a decrease in cellular traction force (12,21,22), the rate of neurite outgrowth (8,23), and the size of growth cones (8). It is accepted that the advance of growth cones is inversely proportional to retrograde F-actin flow that is mediated by myosin activity (24,25). NMM-IIs appear to be responsible for driving F-actin retrograde flow in neuronal cells (20), but the involvement of other myosins also has been suggested (26). NMM-IIB null fibroblasts have defects in directional migration as a consequence of the multiple, unstable and disorganized protrusions of the cell edge; however, the instantaneous rates of cell movement are in the normal range (12).

In comparison with NMM-IIB, relatively less is known about the roles of NMM-IIA. NMM-IIA seems to drive neurite retraction in neuronal cells (27). Antisense oligonucleotide treatment of NMM-IIA induces rearrangement of the actin cytoskeleton and decreases cell-matrix adhesion in neuroblastoma cells (28). A similar phenotype is also observed in Hela cells when a truncated fragment of the myosin IIA heavy chain is over-expressed (29). Knockout of NMM-IIA leads to impaired embryonic cell-cell adhesion, as indicated by the disappearance of E-cadherin and β-catenin from cell-cell adhesion sites (30).

In a previous study, we showed that inhibition of myosin light chain kinase (MLCK) blocked periodic lamellipodial contractions (31), indicating that NMM-II activity is critical for fibroblasts to probe the extracellular substrate during spreading and migration. However, there are some important questions remaining to be addressed. For example, what are the roles of NMM-IIA and NMM-IIB in cell spreading? Does NMM-IIA contribute to cellular traction force? To answer those questions, we have explored the roles of NMM-IIs in several aspects of cell motility including traction force generation, retrograde F-actin flow, and cell spreading in MEF cells. The findings are all consistent with the hypothesis that NMM-IIA has a primary role in developing a coherent, contractile network from one side of the cell to the other.

MATERIALS AND METHODS

Antibodies and materials

Polyclonal rabbit antibodies against the heavy chains of NMM-IIA and NMM-IIB were obtained as a gift from Dr. Robert Adelstein (NIH, Bethesda, MD) and purchased from Covance (Richmond, CA), respectively. Monoclonal antibody against NMM II-B (clone CMII 23) was from Developmental Studies, Hybridoma Bank, (Univ. Iowa, IA). Polyclonal rabbit anti-β-actin antibody was from Abcam (Cambridge, MA). Monoclonal anti-vinculin antibody and LPA were from Sigma (St. Louis, MO). Rhodamine-phalloidin, all fluorophore-conjugated secondary antibodies, and Calcein-AM were from Molecular Probes (Eugene, OR). Blebbistatin and cytochalasin D were from Calbiochem (San Diego, CA). Fibronectin used for coating coverslips and micro-posts was from Roche (Indianapolis, IN). Laminin was from Invitrogen (Carlsbad, CA). GFP (green fluorescent protein) -NMM-IIA and IIB constructs were described elsewhere (22).

Cell culture and transfection

All MEF cell lines were maintained in Dulbecco's modified Eagle medium (DMEM) (Invitrogen) supplemented with 10% NCS except that the medium for the RPTP cell lines was supplemented with 10% FBS. Plasmid transfection was performed with FuGene 6 (Roche) or Nucleofector II (Amaxa, Gaithersburg, MD).

RNAi of nonmuscle NMM-IIA

The pSilencer™ H1-3.1 puro vector (Ambion, Austin, TX) was used to express hairpin short interfering RNA (siRNA) targeting mouse nonmuscle NMM-IIA (accession #: NM_022410). The targeting sequence is: GGTGAAGGTGAACAAGGAC. 48-72 hours after transfection of cells with siRNA expression plasmid, puromycin was added to the medium to eliminate untransfected cells and obtain a survival pool of transfected cells. For clonal stable cell lines, cells were clonally selected in 96-well plates. As control, a plasmid encoding a hairpin siRNA whose sequence is not found in the mouse databases (provided by Ambion) was used.

Western blot

Cell lysates were separated in SDS-PAGE and transferred to Millipore nitrocellulose membranes (Billerica, Massachusetts). Then, the membranes were blocked with blocking solution (10% glycerol, 2% Bio-Rad non-fat dry milk (Hercules, CA) in PBS) overnight at 4°C, followed by incubation with primary antibodies as listed above. Bound primary antibodies were detected by ECL detection (Amersham, Piscataway, NJ). The polyclonal rabbit antibody, not monoclonal antibody, against the heavy chain of NMM-IIB was used in the Western blot analysis.

Coverslip and cell preparation for spreading assays

Coverslips were prepared as previously described (31,32). Cells were detached with trypsin/EDTA and the trypsin was inactivated by 1 mg/ml of soybean trypsin inhibitor (Sigma). The cells were then suspended in DMEM without serum and incubated for 20 min at 37° C. For total internal reflection fluorescence (TIRF) microscopy of cell-spreading experiments, cells were incubated with 0.2 μM Calcein-AM for another 20 min before being plated onto substrates.

Immunofluorescence staining

Cells on coverslips were fixed in 3.7% formaldehyde and permeabilized with 0.1% Triton X-100 and then incubated with primary antibodies in PBS/2% BSA followed by incubation with secondary antibodies. Actin filaments were stained with rhodamine-phalloidin. Epifluorescence and TIRF images were captured on an Olympus IX81 inverted microscope (objectives: Olympus PIanApo 40x/1.35 oil or 60x/1.45 oil; cooled CCD camera: Roper Scientific; imaging software: SimplePCI).

Measurement of traction forces with micro-posts

The polydimethylsiloxane (PDMS) micro-posts were prepared and characterized as described previously (33). The dimension of the PDMS micro-posts was 1 μm in diameter, 2 μm center-to-center, and 6 μm in height. The spring constant of the posts was 1.87 nN/μm. To coat posts with fibronectin, arrays of posts were immersed in 10 μg/ml of fibronectin solution for 1 hour at 37°C and then washed with DPBS. Then, cells were plated on the posts in a 37°C incubator for 90 min. The tips of the posts were visualized with a LUCPIanFI 40x/0.60 air objective in bright-field mode on an IX71 Olympus inverted microscope (cooled CCD camera: Roper Scientific; imaging software: SimplePCI). A multiple-particle tracking program (33) was used to analyze the displacement of the posts. Briefly, this multiple particle-tracking program calculated the position of each post for an acquired image. This routine was based on the fact that, in bright-field microscopy, micro-posts acted as wave-guides and appeared bright whereas the background appeared dark. We were able to identify positions of micro-posts with good accuracy by determining the center of mass of the corresponding bright pixels. To detect deflection of a micro-post, it was necessary to know, in addition to its actual position, the unbent position, which was difficult because micro-posts covered by cells can never be considered as being at rest. To overcome this difficulty, our method relied on the characteristic that the array of micro-posts was an extremely regular hexagonal lattice. While each micro-post in a square array would be the intersection of a row and a column of the matrix, each micro-post belonged to three rows with angles of 60° and 120° between them in a hexagonal lattice. To determine the rest position of a given covered micro-post, the computer program located the positions of the uncovered posts belonging to the same row and fitted them linearly. The unbent position of the pillar was estimated as the intersection of two lines, given by the rows to which it belongs.

The spatial resolution was 5 nm, corresponding to 9 pN force, in the experimental system used in this study. We analyzed the systematic error in force measurement. To obtain it, we selected random areas where there were no cells in the images acquired from independent samples and measured the displacement of micro-posts. The systematic error was 0.0155 nN per post, which was subtracted in the calculation of the cell traction force.

Coupling of fibronectin to beads

100 μl of 2.7-μm magnetic beads (Dynal Biotech.) were washed with 0.1 M carbonate buffer and 0.02 M phosphate buffer sequentially before being incubated in 750 μl of 2% carbodiimide/phosphate buffer for 3 hours at room temperature. The beads were then washed with 0.1 M borate buffer and incubated with 400 μg of albumin from chicken egg white (Sigma). The beads were incubated in 1ml of 0.1 M ethanolamine, washed with 0.02 M phosphate buffer, and biotinylated with 450 μg of NHS-LC biotin (Pierce). The beads were incubated in 500 μl of 10 mg/ml BSA/PBS overnight at 4°C. Then, 30 μl of beads were incubated with 16 μl of 10mg/ml avidin (Molecular Probes) for 30 min at room temperature, washed with BSA/PBS, and incubated with 5 μg of purified biotin-fibronectin for 30 min at room temperature.

Retrograde F-actin flow assay

Cells were plated onto laminin (40 μg/ml) -coated coverslips preloaded with fibronectin-coated 2.7-μm magnetic beads to allow spread at 37°C. 2-second time-lapse images of beads transported centripetally on surface of spreading cells were captured on an IX81 Olympus inverted microscope (objective: Olympus PIanApo 60x/1.45 oil; cooled CCD camera: Roper Scientific; imaging software: SimplePCI).

TIRF microscopy

To study spreading, the entire cell spreading process of cells labeled with Calcein-AM was captured as previously described (32). To follow the dynamics of GFP-NMM-IIA and GFP-NMM-IIB in cells, time-lapse images were captured with a cooled CCD camera (Roper Scientific) attached to an Olympus IX81 inverted microscope (objective: Olympus PIanApo 60x/1.45 oil; imaging software: SimplePCI) coupled to the 488 nm excitation light from an Inova argon-ion laser.

Image analysis of TIRF images and bead movement

To quantify the size of vinculin-containing focal adhesions, a threshold (value depending on individual images) was applied to vinculin TIRF images. “Particle analysis” function in ImageJ was then used to calculate the size (area) of focal adhesions.

To quantify cell spread area and generate a velocity map, sequential TIRF images for the study of cell spreading were analyzed using a method as described elsewhere (34). In detail, time-lapse image sequences were analyzed with Matlab (The Mathworks, Natick, MA). The Expectation-Maximization (35) algorithm was used to calculate the maximum likelihood probability distribution over pixel intensities for each frame, constrained to the functional form of a weighted sum of two normal distributions (one describing a class of foreground pixels at high intensities, the other a class of background pixels at low intensities) (36). The inferred mean intensities were used to perform background subtraction and foreground normalization, allowing for robust handling of varying contrast and brightness between frames. An averaging filter (applied over both space and time) was used to mollify noise in the normalized image sequence; Expectation-Maximization was then re-applied to update pixel intensity model parameters. Given a user-prescribed sensitivity (i.e. relative probability) for assignment to the foreground class, a threshold pixel value was calculated and used to convert the grayscale image sequence to a binary one. The resulting set of foreground pixels defined a simple closed curve delineating the edge of the cell, which was then parameterized by arc length to accommodate cells with non-convex morphologies. For each point on the boundary, the normal velocity was calculated as the ratio of temporal differences in pixel intensities to the magnitude of spatial differences at that point (a simpler case of the vectorial velocity inference problem often addressed by optical flow methods) (37). Results are displayed in color-coded plots, as in Fig. 5 *E-H*, where points on the cell boundary are specified by time (in minutes) and arc length (in microns); red coloring represents protrusion events while blue represents retraction events. Velocities with an absolute value less than 0.5 micron/min are not shown in the plots, as they are not considered to be relevant events. They are reflected as colorless patches among red and blue ones. Plotting velocity as a function of arc length and time gave the dynamic motility pattern of a cell. The area bounded by the cell contour was also calculated and plotted as a function of time.

Kymograph analyses of GFP-NMM-II TIRF images were performed using ImageJ software.

Bead movement on spreading cells was analyzed as following: a custom nano-tracking ImageJ plug-in was used to determine the coordinates of beads in sequential images. Then, the coordinates were loaded to a custom velocity function in Igor software to analyze the instantaneous velocity and the average velocity.

Statistical analysis

All statistical analyses were performed with a student’s t-test tool.

RESULTS

Traction force is reduced in NMM-IIA-knockdown cells

To study the functions of NMM-IIA, we knocked down its expression in MEF cells using plasmid-based RNAi. Several RPTP (namely RPTP$\alpha^{+/+}$ cells described elsewhere (38)) NMM-IIA-knockdown clonal cell lines were generated. They all had similar phenotypes. We focused our further analyses on the RPTP NMM-IIA-knockdown stable line 6 (RPTP-C6) that showed ~85% reduction of NMM-IIA protein levels compared with control cells (Fig. 1 *A*). To investigate the effect of knockdown in different cell backgrounds, we also knocked down NMM-IIA in NIH3T3 cells and studied the NIH3T3 NMM-IIA-knockdown stable line 4 (NIH3T3-C4) (Fig. 1 *A*). The knockdowns were specific since NMM-IIB, β-actin, and vinculin were not affected (Fig. 1 *A*). Furthermore, the control siRNA plasmid had no affect on the expression of those proteins (Fig. 1 *A*). In the rest of the experiments presented here, the control cells for the study of NMM-IIA functions were cells transfected with the control plasmid (designated as RPTP-control or NIH3T3-control) unless specifically noted.

NMM-IIB contributed to traction force in neurons (21) and MEF cells (12,22). It has been proposed that NMM-IIA generated traction force as well. Nonetheless, no direct evidence has been reported yet. To determine whether NMM-IIA contributed to substrate traction force, we used different force sensing substrates. On deformable silicone sheets (39), RPTP-control cells generated more and longer wrinkles than RPTP-C6 cells in the presence of serum 90 min after plating as revealed in Figure S1. The reduction of substrate traction force was also observed in NIH3T3-C4 stable cells compared with NIH3T3-control cells (Fig. S1). This result clearly indicated that NMM-IIA contributed to force generation. For comparison, we also performed the same assay on the NMM-IIB$^{-/-}$ (NMM-IIB knockout) cell line and its control, NMM-IIB$^{+/+}$ cell line (Fig. S1). Both cell lines have no NMM-IIC (12,22). NMM-IIB$^{-/-}$ cells wrinkled less than NMM-IIB$^{+/+}$ cells on silicone sheets (Fig. S1), in agreement with previous studies using collagen gels (22) and deformable polyacrylamide gels (12).

To get a more quantitative measure of the traction forces, we employed deformable arrays of micro-posts as previously described by us (33) and Tan *et al.* (40). The arrays of micro-posts used in this study were 1 μm in diameter and 2 μm center-to-center. Cells only applied traction force to the tips of the posts because they attached and spread on the tips of the posts without spreading down along the posts (em data not shown), as was previously demonstrated using scanning electron microscopy (33). The NMM-II-deficient and control cells were plated on the micro-posts coated with fibronectin in the presence of serum. Cells generated maximal pulling force after 60-120 min on the posts (40). Hence, we plated cells for 90 min, and then imaged the well-spread living cells and the micro-posts (Fig. 1 *B*) for quantification of traction force. As shown in Fig. 1 *B*, the posts were bent inward at the cell edge, indicating that inward pulling forces were exerted on the posts by cells. The magnitude of the deflection of individual posts was obtained by measuring the distance between the deflected position and the resting position of the posts using a custom program (33). By adding up the force applied by the cells on all independently bent posts, we obtained the total cell force. RPTP-C6 cells generated ~53.4% of the force detected in RPTP-control cells (Table 1). NIH3T3-C4 maintained ~41.6% of the traction force of NIH3T3-control cells (Table 1). The average of force generated by those two NMM-IIA-knockdown cell lines was 47.5% of the controls. Thus, loss of ~85% of the NMM-IIA (Fig. 1 *A*) resulted in the loss of ~52.5% of the traction force. Since the NMM-IIA had a similar distribution pattern in control cells and NMM-IIA-knockdown cells (Fig. 2), we assumed that there was a linear relationship between the level of NMM-IIA and its contribution to traction

force. We therefore proportionally calculated the contribution of NMM-IIA to the total cell traction force and found that NMM-IIA was responsible for ~60% of the traction force. On the other hand, comparison of traction force between NMM-IIB$^{+/+}$ cells and NMM-IIB$^{-/-}$ cells revealed that NMM-IIB protein accounted for ~30% of the traction force (Table 1). Thus, NMM-IIA contributes the major fraction of fibroblast traction force. This appeared to agree with what Lo *et al.* previously suggested using two-dimensional polyacrylamide gel surfaces (12).

We also measured the relative force contribution of NMM-IIA and NMM-IIB by knocking down NMM-IIA in NMM-IIB$^{-/-}$ cells to obtain NMM-IIB$^{-/-}$_IIA-knockdown (NMM-IIB$^{-/-}$_IIAKD) cells. This led to the production of ~20% of the cells with two or more nuclei. A similar phenotype was displayed by cells treated with blebbistatin, a specific inhibitor of NMM-IIs (3). In our experiments, we transfected NMM-IIB$^{-/-}$ cells with NMM-IIA siRNA expression plasmid and then enriched the population of transfected cells by antibiotic selection for three days. Thus, a transient pool of NMM-IIB$^{-/-}$_IIAKD cells was obtained. Immunoblotting (Fig. 1 *C*) showed that only ~20% of control levels of NMM-IIA was present in NMM-IIB$^{-/-}$_IIAKD cells. Force measurement with micro-post assay revealed that knockdown of NMM-IIA in NMM-IIB$^{-/-}$ cells led to a decrease of traction force. Subtraction of the force in NMM-IIB$^{-/-}$_IIAKD (~46 nN) cells from that in NMM-IIB$^{-/-}$ cells (~123 nN) (Table 1) gave ~77 nN, which was the force value contributed by ~80% of the NMM-IIA. Proportional calculation of force indicated that the contribution of NMM-IIA to total force was ~97 nN, which was ~55% of the force seen in NMM-IIB$^{+/+}$ cells. Thus, NMM-IIA was again shown to contribute to the major fraction of fibroblast traction force.

Because force measurements were conducted in the presence of serum, we tested if the activation level of NMM-II accounted for the differences seen in the level of traction force. To maximally activate myosin contraction, we added external lysophosphatidic acid (10 μM of LPA) to NMM-IIB$^{+/+}$, NMM-IIB$^{-/-}$, and NMM-IIB$^{-/-}$_IIAKD cells. About the same levels of traction force were generated before and after 30-min of exposure to external LPA (Table 1). We did not observe noticeable differences in cell traction force after 5, 10, 15, 20 and 30 min exposure to external LPA (data not shown). This experiment indicated that NMM-II was fully activated in the presence of serum and the traction force level was indeed primarily dependent upon the NMM-II protein level. Since NMM-IIB/-_IIAKD cells still retained ~25.8% of the traction force seen in NMM-IIB$^{+/+}$ cells, we inhibited NMM-II activity in NMM-IIB$^{+/+}$ cells with 50 μM of blebbistatin for 40 min and analyzed the force output. We found that the blebbistatin-treated NMM-IIB$^{+/+}$ cells still retained ~21.3% of the force (Table 1). Similar to cells treated with the general inhibitor of myosin ATPase, 2,3-butanedione-2-monoxime (BDM) (40), cells treated with blebbistatin might have residual myosin activity. That could include the residual activity of NMM-II and/or the activity of other myosins. To test this possibility and determine the lowest traction force values, we disrupted the actin cytoskeleton of NMM-IIB$^{+/+}$ cells by treating them with 1 μg/ml of cytochalasin D for 20 min and found that the traction force was down to 21 ± 7.1 nN, 11.8% of untreated NMM-IIB$^{+/+}$ cells (Table 1). This suggests that the NMM-IIB$^{+/+}$ cells likely retained residual NMM-II activity after treatment with 50 μM of blebbistatin in our experiments. We also measured the traction force in RPTP-control and NIH3T3-control cells treated with 1 μg/ml of cytochalasin D. They produced 31 ± 8.0 nN (8.2% of untreated RPTP-control cells) and 28 ± 6.5 nN (10.1% of untreated NIH3T3-control cells), respectively. Those force values were fairly close to the force generated by NMM-IIB$^{+/+}$ cells treated with cytochalasin D. The measured force in cells treated with cytochalasin D could be due to

membrane tension, adhesion-generated forces, or limited sensitivity at low force measurement in our system. This remains to be determined.

Thus, we concluded that, based on the force measurements with three different MEF cell lines, NMM-IIA contributed ~60% and NMM-IIB contributed ~30% of the total traction force. The remainder ~10% was from other factors.

NMM-IIA regulates formation of stress fibers and focal adhesions

The actomyosin system was found to be essential for the formation of focal contacts (41-45). Previous studies of NMM-IIA in other cells lines including Hela cells (29) and neuroblastoma cells (28) showed that NMM-IIA regulates the formation of stress fibers and focal adhesions. This prompted us to examine the focal adhesions and stress fibers in NMM-IIA-knockdown MEF cells. MEF cells were spread on a fibronectin substrate for 90 min before fixation and immunostaining because, at this time point, normal fibroblast cells were able to polarize and form focal adhesions and stress fibers. Staining of NMM-IIA showed that RPTP-C6 cells had significantly less NMM-IIA than RPTP-control cells (Fig. 2), which fitted with the previous immunoblotting (Fig. 1 *A*). The suppression of NMM-IIA led to a reduction of stress fibers in RPTP-C6 (Fig. 2 *F*) cells. The remaining NMM-IIA in RPTP-C6 cells (Fig. 2 *E*) formed a punctate pattern in stress fibers and lateral cortex, similar to RPTP-controls (Fig. 2 *A*). This was also confirmed with confocal microscopy (data not shown). In addition to a reduced number of stress fibers, RPTP-C6 cells appeared to have increased dot-like actin staining concentrated in the perinuclear area. The increase of dot-like actin was probably a result of increased disassembly of stress fibers caused by the deficiency of NMM-IIA in cells (28). Concomitantly, the size of the focal adhesions as indicated by vinculin staining was clearly smaller in RPTP-C6 cells (Fig. 2 *G*) than in RPTP-control cells (Fig. 2 *C*). The same phenotype was also observed when NMM-IIA was depleted in NIH3T3 cells (Fig. 2 *I-P*).

Focal adhesions were the sites where cells primarily transmitted force to the substrate (46). In light of this, we quantified and compared the size of focal adhesions in NMM-IIA-knockdown cells *versus* control cells. The vinculin TIRF images were used to quantify the focal adhesion size in cells because we found there was interference from the perinuclear region when epifluorescent and confocal images were used for analysis. Since both focal complexes and focal adhesions contained vinculin (47), we used a size filter to discriminate between focal complexes and focal adhesions. Focal complexes were defined as small dots with an apparent diameter of ~0.7 μm, similar to the size of focal complexes reported elsewhere (48). We quantified focal adhesions in control *versus* NMM-IIA-knockdown cells and found that RPTP-C6 and NIH3T3-C4 cells had ~34% and ~25% of the focal adhesion area of their respective control cells (also see Fig. 3). As demonstrated above with micro-posts assay, RPTP-C6 and NIH3T3-C4 cells retained ~53.4% and ~41.6% force of their control cells (Table 1). Thus, the ratios of the loss of focal adhesions to the loss of traction force were ~1.37 and ~1.27 for PTP-C6 and NIH3T3-C4, respectively. Those ratios were close and indicated that the size of focal adhesions positively correlates with the force (40,46,49).

Retrograde F-actin flow depends on NMM-IIA

Retrograde F-actin flow is regulated by myosin-based contractile force in a variety of cell types (20,25,50,51). Therefore, it is logical to examine the influence of force-producing NMM-IIs on the retrograde F-actin flow in MEF cells. To this end, we analyzed the centripetal movement of fibronectin-coated beads on the surface of spreading MEFs. Bead movement on the cell surface has been shown to reflect the rearward movement of the actin cytoskeleton (20,24,31). We chose to analyze the bead movement in the 3.0-μm-wide lamellar region that was

~2.0 μm away from the cell leading edge (Fig. 4, *A* and *B*) because there was little or no NMM-II in the lamellipodium (Fig. 6) (52) and the average width of lamellipodium in MEFs was ~ 1-2 μm (31). In these experiments, cells were plated onto laminin-coated coverslips pre-loaded with fibronectin-coated beads. As cells spread on the substrate, they picked up the beads and transported them centripetally (Fig. 4, *A* and *B*) (20,25). Most beads were transported steadily towards the center of cells and stopped in the perinuclear area. Occasionally, beads stopped moving after passing the lamellipodium and those beads were not counted. More beads stopped moving on NMM-IIA-knockdown cells than controls. For the purpose of comparison, we analyzed the beads that were picked up by the cells reaching the late spreading stage where cells were very active but the cell edge remained relatively in equilibrium. Both control cells (i.e., RPTP-control in Fig. 4 *B*) and NMM-IIA-knockdown cells (i.e., RPTP-C6 in Fig. 4 *B*) could transport beads to the perinuclear region eventually, but velocity analysis revealed that beads moved at a lower velocity on RPTP-C6 cells (21.0 ± 5.7 nm/sec, n = 15 beads, 12 cells) than on RPTP-control cells (58.6 ± 11.9 nm/sec, n = 12 beads, 10 cells) (Fig. 4 *C*; Supplementary Movies 1 and 2). This indicated that NMM-IIA contributed significantly to retrograde F-actin flow and that NMM-IIB was not able to compensate for the loss of NMM-IIA in powering retrograde F-actin flow during early spreading period.

Did NMM-IIB drive actin flow as well? To compare the roles of NMM-IIA and NMM-IIB in F-actin flow, we first investigated the effect of ablation of NMM-IIB on the retrograde F-actin flow in MEF cells. Surprisingly, the rearward velocity of fibronectin-coated beads on NMM-IIB$^{-/-}$ cells (59.0 ± 25.0 nm/sec, n = 25 beads, 23 cells, Fig. 4 *D*; Supplementary Movie 3) was similar to that on NMM-IIB$^{+/+}$ cells (57.5 ± 20.0 nm/sec, n = 26 beads, 18 cells, Fig. 4 *D*; Supplementary Movie 4). When NMM-IIB$^{-/-}$_IIAKD cells were analyzed, they displayed reduced capacity to transport beads (24.0 ± 10.1 nm/sec, n = 29 beads, 20 cells, Fig. 4 *D*; Supplementary Movie 5). This further supported the hypothesis that NMM-IIA, not NMM-IIB, was involved in retrograde F-actin transport in MEF cells.

NMM-IIA impedes early cell spreading

It was generally accepted that there was an inverse relationship between retrograde F-actin flow and cell protrusion (24,50). If NMM-II powered retrograde F-actin flow, then the cell protrusion should be augmented when NMM-II was depleted. Consistent with this concept was the finding that cells spread larger when NMM-II activity was inhibited by pharmacological regents (4). In light of this, we have followed and analyzed the spreading processes of Calcein AM-labeled MEF cells on fibronectin substrates to dissect the roles of NMM-IIA and NMM-IIB in cell spreading using the TIRF microscope system as previously described (32) (see Fig. 5 *A* for selected time-lapse TIRF images of a control MEF cell spreading on fibronectin). Time 0 refers to the moment at which cell spread area was large enough (~100 μm^2) to be analyzed (32). Typically, the average time for MEF cells to reach to their fully spread stage on fibronectin was ~16 min in our experiments. We examined the role of NMM-IIB in cell spreading by comparing NMM-IIB$^{+/+}$ and NMM-IIB$^{-/-}$ MEFs. NMM-IIB$^{+/+}$ (1254 ± 301 μm^2 (average ± standard variation), n = 30 cells) and NMM-IIB$^{-/-}$ (1265 ± 446 μm^2, n = 34 cells) cells had similar spread area after spreading for 16 min (Fig. 5 *B*), which indicated that NMM-IIB seemingly had no influence on cell spread area. In contrast, the depletion of NMM-IIA resulted in a significant increase in the spread area. The RPTP-control cells spread slower than the RPTP-C6 cells (Fig. 5 *C*). After the initial spreading process, the RPTP-control cells spread to a smaller area than the RPTP-C6 cells (Fig. 5 *C*). The average rate of increase in cell spread area for RPTP-C6 cells was 150 ± 32.6 μm^2/min (n = 40 cells), or ~1.54-fold faster than that of RPTP-control cells (97.5 ±

24.2 μm^2/min, n = 41 cells). Correspondingly, the average of cell spread area of RPTP-C6 (2360 ± 298 μm^2) was ~1.47-fold as large as that (1610 ± 182 μm^2) of RPTP-control cells after 16 min. To see whether depletion of NMM-IIA caused other MEF cell lines to spread faster, we examined NIH3T3-control and NIH3T3-C4 cells. The average time for NIH3T3-C4 cells to reach to their fully spread stage was ~16 min. However, it took ~40 min on average for NIH3T3-contols to fully spread to a smaller area. For comparison of early cell spreading within the same time scale, we quantified the first 16 min spreading of NIH3T3-control and NIH3T3-C4 cells. NIH3T3-C4 cells spread (113.1 ± 26.0 μm^2/min, n = 36 cells) ~2.7-fold faster than NIH3T3-control cells (41.8 ± 19.8μm^2/min, n = 38 cells), and the spread area of NIH3T3-C4 cells (1910 ± 387 μm^2) was ~2.5-fold larger than NIH3T3-control cells (749 ± 150 μm^2). All the above differences were significant (t-test, $p < 0.001$). The same spreading assay was also applied to at least four other NMM-IIA knockdown stable cell lines and they also spread to a larger area than controls (data not shown).

The details of cell edge protrusion/retraction in control and NMM-IIA-knockdown MEF cells could be visualized in velocity maps (Fig. 5, *E-H*). In the first several (~4.5) minutes, protrusion of the cell edge was dominant in both RPTP-control cells (Fig. 5 *E*) and RPTP-C6 cells (Fig. 5 *F*). The velocity of cell edge protrusion (red color) was similar in both cell lines during this period; but between 4.5 min to 6 min, RPTP-C6 cells clearly had a higher velocity of edge protrusion than RPTP-controls. At later times (from ~6 to ~16 min), RPTP-C6 cells had obvious longer and more extensive protrusion events than RPTP-control cells although the highest velocity of local edge protrusion was similar. In RPTP-C6 cells, the fraction of the edge that was stationary (colorless patches among red and blue ones in velocity plots) was smaller than in RPTP-control cells, indicating that the rate of area increase was greater. In terms of edge retraction (blue color), both cell lines had a similar velocity distribution of edge retraction events. When NIH3T3-control cells (Fig. 5 *G*) were compared with NIH3T3-C4 cells (Fig. 5 *H*), the controls had a much slower velocity of edge protrusion as well as shorter and smaller protrusion events through almost the entire spreading process. Again, the distributions of retraction events were comparable in NIH3T3-control and NIH3T3-C4 cells. Thus, the instantaneous process of edge movement was dramatically greater in extent and velocity when NMM-IIA was depleted.

Given the above findings in force and retrograde F-actin flow analyses, we suggest that NMM-IIA, not NMM-IIB, powers early cytoplasmic contractions that inhibited the rate of spreading and resulted in a decreased spread area at early times.

NMM-IIA has different distribution and dynamics from NMM-IIB in spreading MEF cells

Since NMM-IIA and NMM-IIB displayed differential cellular functions in our studies, we investigated whether NMM-IIA and NMM-IIB had different distributions and dynamics in spreading MEF cells. To this end, we first examined GFP-NMM-IIA and GFP-NMM-IIB adjacent to the interface of RPTP MEF cells with extracellular substrate using TIRF microscopy. Both NMM-IIA and NMM-IIB (Fig. 6 *A*) were in discrete clusters. There were few or no NMM-II clusters in the lamellipodia of spreading RPTP cells. NMM-IIA was extremely rich in the front lamellar region but present in inner regions of the cell at a very low density (Fig. 6 *A*). In contrast, NMM-IIB was seen primarily in the perinuclear region of cells (Fig. 6 *A*). Close examination of sequential TIRF images demonstrated that both NMM-II isoforms underwent rearward movement (Supplementary Movies 6 and 7). In the inner regions, NMM-II clusters showed several different movement behaviors. Clusters showed irregular, slow rearward movement (even forward movement occasionally) with occasional lateral movement or stationary periods. In the front lamellar regions, clusters clearly moved rearward and the

velocities of movement of NMM-IIA and NMM-IIB clusters were different. To compare their velocities, we analyzed kymographs of GFP-NMM-IIA and GFP-NMM-IIB clusters in the periphery of front lamellar regions (Fig. 6 *B*) and calculated velocities from the slopes. NMM-IIA (0.56 ± 0.11 μm/min, Fig. 6 *C*, n = 50 clusters, 6 cells) moved rearward significantly faster than NMM-IIB (0.32 ± 0.07 μm/min, Fig. 6 *C*, n = 40 clusters, 5 cells), in agreement with earlier studies in endothelial cells (14).

TIRF only detects fluorescence within a few hundred nanometers of the substrates. To examine whether NMM-IIA and NMM-IIB were in the area not adjacent to the cell-substrate contact surface, we spread RPTP MEF cells for ~15 min, immunostained for NMM-IIA and NMM-IIB and performed epifluorescent microscopy. Although epifluorescent images could not tell us whether NMM-IIs were in the cortex or in other areas of cytoplasm, it was important for us to determine whether we could see similar distribution patterns of NMM-IIA and NMM-IIB throughout entire cell space as those we saw with TIRF microscopy. Epifluorescent images (Fig. 6 *D*) showed that NMM-IIA and NMM-IIB had punctate distributions outside of the lamellipodium. Interestingly, NMM-IIA was relatively uniformly distributed in a 3-10 μm ring extending from the back of the lamellipodium inward. To confirm TIRF and epifluorescent images, confocal microscopy was carried out. The confocal Z-stacks (Fig. S2), together with the TIRF and epifluorescent images, indicated that NMM-IIA accumulated at high density near the cell-substrate interface in the outer portion of the lamellar region. In the inner region of cells, NMM-IIA was concentrated above the cell-substrate interface in a cortical distribution. On the other hand, NMM-IIB was concentrated in perinuclear regions in epifluorescent and TIRF images (Fig. 6) as well as confocal Z-stacks (Fig. S2). The dramatic differences in NMM-IIA and NMM-IIB distributions were consistent with their different functional activities.

DISCUSSION

We find that ~90% or more of the traction force generated by MEF cells on a fibronectin-coated substrate is lost with the removal of NMM-IIs. NMM-IIA is responsible for the majority (~60%) of the force whereas NMM-IIB accounts for a smaller faction (~30%). Our force analyses are in agreement the work from Lo *et al.*, who demonstrated that NMM-IIB$^{-/-}$ fibroblasts retained the majority of the traction force on flexible polyacrylamide substrates (12). This is consistent with earlier observations of functional differences between the two NMM-II isoforms (12,13,53,54). In addition, there is a larger cell spread area on fibronectin at early times with the loss of NMM-IIA but not NMM-IIB. NMM-IIA may be responsible for pulling in the actin cytoskeleton and counteracting cell spreading. In support of this, the rate of edge movement outward is increased in NMM-IIA-knockdown cells. Further, the rate of inward actin cytoskeleton transport is decreased dramatically in NMM-IIA-knockdown cells. Analyses of GFP-NMM-IIA and GFP-NMM-IIB clusters indicate that NMM-IIA moves inward more rapidly than NMM-IIB. Thus, we favor the hypothesis that contraction of NMM-IIA is a major factor in organizing a coherent cytoskeleton that is able to generate force from one side of the cell to the other by pulling the actin cytoskeleton inward.

Several lines of evidence indicate that NMM-IIs are major force generators in nonmuscle cells although they are not the only force generators needed for cell migration. In the amoeboid cells of *Dictyostelium d.*, migration in the absence of NMM-II is greatly slowed when the cells need to generate force to move (55,56). In NMM-IIB$^{-/-}$ MEF cells, there is considerable evidence of decreased force generation from other groups (12,21) and in this study (Table 1). However, NMM-IIA is the major contributor to mechanical force generation in MEF cells, responsible for ~60% of the total traction force. Interestingly, NMM-IIB$^{-/-}$_IIAKD cells still generated 25.8% of force generated by NMM-IIB$^{+/+}$ cells. The remaining ~20% of NMM-IIA expressed in NMM-IIB$^{-/-}$_IIAKD cells may be responsible for about half of the force. Some of the measured force may be due to the adhesion of the cell to the post tips and the fluctuations in cell volume without a significant myosin contribution, since significant forces (~10% of control) are observed after cytochalasin D inhibition of actin filament assembly. When exposing the cells to LPA, we found that there was still decreased traction force generated by NMM-IIA-knockdown cells, indicating the overall contractility of these cells is dependent upon the level of NMM-IIA and not the amount of activation. There are several caveats to the quantification of total cell force such as cell area or the expression level of other myosins; however, we only find inward contractile forces and not extensile forces (for all cells). After taking into account the ~10% of the post force generated by adherence and possibly volume changes, we estimate that ~90% or more of the fibroblast tension on micro-posts is due to NMM-IIs and the contribution of other myosins is not above the errors in our measurements (estimated at about 5 nN).

There are additional consequences to the loss of NMM-IIA related to the rearward flow of F-actin and the spreading process. As others have observed for cells strongly adherent to the substrate, the loss of the retrograde force leads to an increase in cell extension, consistent with the “clutch” hypothesis (50,57,58). NMM-IIA-based contractile force leads to retrograde slipping of actin cytoskeleton with respect to focal adhesions as well as expansion of those contacts. When force is reduced and the adhesive contacts remain, there is reduced retrograde F-actin flow. Since actin assembly and retrograde F-actin flow are uncoupled processes (25), the net effect of reduced retrograde F-actin flow and sustained actin assembly is an increase in cell protrusion rate (Fig. 5). The increased area with NMM-IIA depletion is found only at early times after spreading and at later times (e.g. 90 min after plating) the cells have an area similar to

control cells (Fig. 2). One explanation for this change is that the cells in a polarized phase do not have the same organization of NMM-IIA (59). An example of the changes in myosin organization in different phases of motility is the redistribution of NMM-IIB to the leading lamellipodia when cells are pulling on collagen fibers in 3-dimensional (3-D) substrates as opposed to moving on 2-dimensional (2-D) collagen-coated glass (22). Thus, we suggest that NMM-IIA is a primary motor for actin rearward movement that inhibits cell spreading in the contractile phase of cell spreading on 2-D surfaces (31).

A number of earlier studies are consistent with our observation of the roles of NMM-IIA in spreading MEFs. Inhibition of NMM-II activity with the protein kinase inhibitor staurosporine or the MLCK inhibitor KT5926 facilitates fibroblast spreading (4) and inhibits F-actin flow in the cell center of sea urchin coelomocytes (51). Inhibition of myosin activity by NEM-inactivated myosin S1 fragments or by BDM enhances growth cone advance of *Aplysia* bag cell neurons (25). Further support is from a very recent report by Medeiros *et al.* who reported that F-actin retrograde flow is remarkably decreased in *Aplysia* bag cell neurons treated with blebbistatin (60). One important part of our findings is that we have addressed that NMM-IIA, not NMM-IIB, primarily regulates cell protrusion and retrograde F-actin flow of spreading MEF cells. In agreement with this idea is that over-expression of NMM-IIA does not rescue the change of growth cone turning caused by the loss of NMM-IIB in explanted neurons of NMM-IIB knockout mice (61). These findings support the concept that NMM-IIA and NMM-IIB have distinct functions.

In conjunction with the reduction of force in NMM-IIA-deficient MEF cells, there are fewer focal adhesions and stress fibers, as expected from previous studies demonstrating that force correlates with the size of focal adhesions (40,46). NMM-IIA is the major force generator and is essential for the development of focal adhesions and stress fibers (Fig. 2) (28,29). NMM-IIB generates some mechanical force as well (Table 1) (12) but seems not to be involved in the development of focal adhesions and stress fibers (12). This is consistent with the picture that NMM-IIB may be more involved in local force generation on 2-D substrates or 3-D force generation in lamellipodial regions (22) whereas NMM-IIA may function primarily in 2-D force generation from one side to the other in fibroblasts.

Different distributions as well as different activity levels may account for the different functional roles of NMM-IIA and NMM-IIB. One possibility is that NMM-IIA may connect the central cytoskeleton to the peripheral actin cytoskeleton in cells spreading on 2-D surfaces, which is supported by the observation that, near the fibronectin-coated glass substrate, NMM-IIA accumulates at high density in the front portion of the lamellar region, whereas in regions around the nucleus, NMM-IIA is rich above the nucleus in the cortical region of cells (Fig. 6 and Fig. S2). The peripheral actin filaments that are transported rearward by NMM-IIA are presumably linked to the other parts of the cell by a coherent cytoskeleton in which NMM-IIA plays a significant role as a crosslinker. In early cell spreading where substrate contacts have not matured, the loss of NMM-IIA will weaken the coherence, resulting in accelerated and uncoordinated cell spreading. Unlike NMM-IIA, NMM-IIB seems not to be the driving force for the rearward F-actin transport. NMM-IIB is localized much more in perinuclear regions than in other cytoplasmic areas in early spreading cells (Fig. 6 and Fig. S2). It is tempting to argue that NMM-IIB might be close to substrate contacts throughout the cell and therefore no detectable difference in retrograde flow was detected between NMM-IIB$^{+/+}$ and NMM-IIB$^{-/-}$ cells using the bead assay and yet it does contribute to traction forces and peripheral contractions in spreading. On 2-D substrates, NMM-IIB may be largely in an inactive pool that is stored in the perinuclear

region and then recruited for peripheral contractions or fiber pulling (Fig. 6). The higher concentrations of NMM-IIA above the surface further supports our hypothesis that it is primarily involved in the radial contraction of peripheral actin and developing a cohesive cytoskeleton on 2-D surfaces.

The distinct functions of MM-IIA and NMM-IIB are also perhaps related to their different biochemical characteristics, interaction partners, and dynamics. NMM-IIA has about a three-fold greater actin-activated ATPase rate and translocation rate for actin filaments than NMM-IIB does (53). Accordingly, the kinetic mechanisms for NMM-IIA and NMM-IIB are significantly different. NMM-IIA has a low duty ratio characteristic similar to that of muscle myosin and therefore is better structured for contraction over longer distances (9,54). Indeed, the distribution of NMM-IIA is indistinguishable from smooth muscle myosin II when both were micro-injected into endothelial cells (14). In contrast, NMM-IIB has a moderately high duty ratio (9,54). Therefore, it might be mainly involved in maintaining cell tension in a static manner (9). Those biochemical properties fit well with our hypothesis that NMM-IIA, but not NMM-IIB, pulls the inward flow of lamellar actin network during cell spreading on 2-D. Moreover, both NMM-IIs have different protein interaction partners (16-19). As further support, the studies of NMM-IIA and NMM-IIB dynamics in spreading MEF cells (Fig. 6) and migrating endothelial cells (14) demonstrate that NMM-IIB clusters undergo slower rearward movement than NMM-IIA clusters, which seems consistent with NMM-IIB being more involved in static maintenance of tension. There are at least two possible scenarios where NMM-IIB may function on 2-D substrates. In the first scenario, the perinuclear NMM-IIB, by generating tension, may mechanically participate in directing the orientation of nucleus or hold the nucleus in place during cell spreading, e.g. the NMM-II activity that is involved in reorientation of nucleus in migrating cells (62). The NMM-IIB at the lamellar margin may mechanically coordinate the lateral protrusion activities of cell edge (12), but with no obvious effects on cell spread area. The NMM-IIB at the lamellar margin also may be involved in the periodic lamellipodial contractions as described in our previous study (31). In light of the observation that MLCK travels to the proximal boundary of lamellipodium from the leading edge during periodic lamellipodial contractions as a component of a signal complex (31), it is tempting to speculate that NMM-IIB (and/or NMM-IIA) may be critical for the continuance of periodic contraction cycles. In the second scenario, NMM-IIB may exhibit cell motility state-dependent roles. At early cell-spread times, NMM-IIB may primarily modulate vesicle trafficking (63) and may be rarely involved in cell edge protrusion or retraction in early spreading cells. However at later times, NMM-IIB may significantly regulate cell motility, for instance, by stabilizing the polarity of MEF cells (12) or contracting the actin cytoskeleton for tail detachment in migrating cells (13). It seems unlikely that NMM-IIB contributes to actin flow at later times because the rearward F-actin flow in the tail of locomoting *Dictyostelium* is NMM-II-independent (64) and the functional loss of NMM-IIB does not change the rearward actin flow in MEF cells on a 2-D collagen substrate (22).

In cells that are spread on 2-D surfaces, NMM-IIA appears to have an important role in developing a coherent cytoskeleton that generates force on the substrate. If we consider the fact that traction force is greater with greater length of substrate contact, then the increase in spread area with depletion of NMM-IIA may partially compensate for the loss of force. However, the increased spread area with NMM-IIA depletion highlights its role in contracting the cell cytoskeleton. To contract the cytoskeleton, NMM-IIA forms filaments at the periphery that then move inward and disassemble. Such a dynamic cycle is necessary to enable the cell to continue to generate force when actin filaments are assembling in the periphery, moving inward and

disassembling. The sites of NMM-IIA and NMM-IIB filament assembly are distinct and mainly lie in the lamellar regions behind the lamellipodia. Thus, the peripheral actin can be drawn inward by the periodic assembly of NMM-II filaments in lamellar region. How mechanical force plays a role in modulating NMM-IIA filament assembly and in signaling pathways (48) is currently unclear. However, these observations indicate that NMM-IIA has a very critical role in developing contractile traction forces of cells at several different levels.

Note added. During the revision of this manuscript, Betapudi *et al*. published observations of the roles of nonmuscle myosin II isoforms in MDA-MB-231 breast cancer cell spreading and migration (Betapudi, V., L. S. Licate, and T. T. Egelhoff. Cancer Res. 2006. 66:4725-4733). They found that depletion of NMM-IIA leads to an increase (37% larger than controls) of cell spread area 60 min after plating, which is in agreement with our finding reported in this study. However, their finding that depletion of NMM-IIB decreases (27% smaller than controls) cell spreading does not match our observation in MEFs. They suggested that NMM-II contributes to generation of protrusive forces in these cells and that NMM-IIB facilitates cell lamellar protrusion. We did not observe outward pushing of micro-posts at cell edge by fibroblasts plated for 90 min or 60 min. The discrepancy between their observations and ours about the effect of NMM-IIB on cell area may be due to the different distributions of NMM-IIs in the different cell types. Both NMM-IIA and NMM-IIB are preferentially localized to the lamellar margin in MDA-MB-231 breast cancer cells, which is different from those in spreading MEFs (Fig. 6 in this study).

ACKNOWLEDGEMENTS

We thank Benjamin J. Dubin-Thaler for the help in image processing, Olivier Rossier and Nils Gauthier for the valuable comments for the manuscript, and Harry Xenias and other people in the laboratory of Michael P. Sheetz for their excellent assistance. This work was supported by a NIH grant to Michael P. Sheetz (GM-36277). The authors have no conflict of interest.

REFERENCES

1. Sellers, J. R. 2000. Myosins: a diverse superfamily. Biochim Biophys Acta 1496:3-22.

2. Rosenblatt, J., L. P. Cramer, B. Baum, and K. M. McGee. 2004. Myosin II-dependent cortical movement is required for centrosome separation and positioning during mitotic spindle assembly. Cell 117:361-372.

3. Straight, A. F., A. Cheung, J. Limouze, I. Chen, N. J. Westwood, J. R. Sellers, and T. J. Mitchison. 2003. Dissecting temporal and spatial control of cytokinesis with a myosin II Inhibitor. Science 299:1743-1747.

4. Wakatsuki, T., R. B. Wysolmerski, and E. L. Elson. 2003. Mechanics of cell spreading: role of myosin II. J Cell Sci 116:1617-1625.

5. van Leeuwen, F. N., S. van Delft, H. E. Kain, R. A. van der Kammen, and J. G. Collard. 1999. Rac regulates phosphorylation of the myosin-II heavy chain, actinomyosin disassembly and cell spreading. Nat Cell Biol 1:242-248.

6. Arthur, W. T., L. A. Petch, and K. Burridge. 2000. Integrin engagement suppresses RhoA activity via a c-Src-dependent mechanism. Curr Biol 10:719-722.

7. Totsukawa, G., Y. Wu, Y. Sasaki, D. J. Hartshorne, Y. Yamakita, S. Yamashiro, and F. Matsumura. 2004. Distinct roles of MLCK and ROCK in the regulation of membrane protrusions and focal adhesion dynamics during cell migration of fibroblasts. J Cell Biol 164:427-439.

8. Tullio, A. N., P. C. Bridgman, N. J. Tresser, C. C. Chan, M. A. Conti, R. S. Adelstein, and Y. Hara. 2001. Structural abnormalities develop in the brain after ablation of the gene encoding nonmuscle myosin II-B heavy chain. J Comp Neurol 433:62-74.

9. Golomb, E., X. Ma, S. S. Jana, Y. A. Preston, S. Kawamoto, N. G. Shoham, E. Goldin, M. A. Conti, J. R. Sellers, and R. S. Adelstein. 2004. Identification and characterization of nonmuscle myosin II-C, a new member of the myosin II family. J Biol Chem 279:2800-2808.

10. Rochlin, M. W., K. Itoh, R. S. Adelstein, and P. C. Bridgman. 1995. Localization of myosin II A and B isoforms in cultured neurons. J Cell Sci 108 (Pt 12):3661-3670.

11. Maupin, P., C. L. Phillips, R. S. Adelstein, and T. D. Pollard. 1994. Differential localization of myosin-II isozymes in human cultured cells and blood cells. J Cell Sci 107 (Pt 11):3077-3090.

12. Lo, C. M., D. B. Buxton, G. C. Chua, M. Dembo, R. S. Adelstein, and Y. L. Wang. 2004. Nonmuscle myosin IIb is involved in the guidance of fibroblast migration. Mol Biol Cell 15:982-989.

13. Kolega, J. 2003. Asymmetric distribution of myosin IIB in migrating endothelial cells is regulated by a rho-dependent kinase and contributes to tail retraction. Mol Biol Cell 14:4745-4757.

14. Kolega, J. 1998. Cytoplasmic dynamics of myosin IIA and IIB: spatial 'sorting' of isoforms in locomoting cells. J Cell Sci 111 (Pt 15):2085-2095.

15. Saitoh, T., S. Takemura, K. Ueda, H. Hosoya, M. Nagayama, H. Haga, K. Kawabata, A. Yamagishi, and M. Takahashi. 2001. Differential localization of non-muscle myosin II isoforms and phosphorylated regulatory light chains in human MRC-5 fibroblasts. FEBS Lett 509:365-369.

16. Obungu, V. H., A. Lee Burns, S. K. Agarwal, S. C. Chandrasekharapa, R. S. Adelstein, and S. J. Marx. 2003. Menin, a tumor suppressor, associates with nonmuscle myosin II-A heavy chain. Oncogene 22:6347-6358.

17. Huang, H., M. Paliouras, I. Rambaldi, P. Lasko, and M. Featherstone. 2003. Nonmuscle myosin promotes cytoplasmic localization of PBX. Mol Cell Biol 23:3636-3645.

18. Krzewski, K., X. Chen, J. S. Orange, and J. L. Strominger. 2006. Formation of a WIP-, WASp-, actin-, and myosin IIA-containing multiprotein complex in activated NK cells and its alteration by KIR inhibitory signaling. J Cell Biol 173:121-132.

19. Clark, K., M. Langeslag, B. van Leeuwen, L. Ran, A. G. Ryazanov, C. G. Figdor, W. H. Moolenaar, K. Jalink, and F. N. van Leeuwen. 2006. TRPM7, a novel regulator of actomyosin contractility and cell adhesion. Embo J 25:290-301.

20. Brown, M. E. and P. C. Bridgman. 2003. Retrograde flow rate is increased in growth cones from myosin IIB knockout mice. J Cell Sci 116:1087-1094.

21. Bridgman, P. C., S. Dave, C. F. Asnes, A. N. Tullio, and R. S. Adelstein. 2001. Myosin IIB is required for growth cone motility. J Neurosci 21:6159-6169.

22. Meshel, A. S., Q. Wei, R. S. Adelstein, and M. P. Sheetz. 2005. Basic mechanism of three-dimensional collagen fibre transport by fibroblasts. Nat Cell Biol 7:157-164.

23. Wylie, S. R., P. J. Wu, H. Patel, and P. D. Chantler. 1998. A conventional myosin motor drives neurite outgrowth. Proc Natl Acad Sci U S A 95:12967-12972.

24. Lin, C. H. and P. Forscher. 1995. Growth cone advance is inversely proportional to retrograde F-actin flow. Neuron 14:763-771.

25. Lin, C. H., E. M. Espreafico, M. S. Mooseker, and P. Forscher. 1996. Myosin drives retrograde F-actin flow in neuronal growth cones. Neuron 16:769-782.

26. Diefenbach, T. J., V. M. Latham, D. Yimlamai, C. A. Liu, I. M. Herman, and D. G. Jay. 2002. Myosin 1c and myosin IIB serve opposing roles in lamellipodial dynamics of the neuronal growth cone. J Cell Biol 158:1207-1217.

27. Wylie, S. R. and P. D. Chantler. 2003. Myosin IIA drives neurite retraction. Mol Biol Cell 14:4654-4666.

28. Wylie, S. R. and P. D. Chantler. 2001. Separate but linked functions of conventional myosins modulate adhesion and neurite outgrowth. Nat Cell Biol 3:88-92.

29. Wei, Q. and R. S. Adelstein. 2000. Conditional expression of a truncated fragment of nonmuscle myosin II-A alters cell shape but not cytokinesis in HeLa cells. Mol Biol Cell 11:3617-3627.

30. Conti, M. A., S. Even-Ram, C. Liu, K. M. Yamada, and R. S. Adelstein. 2004. Defects in cell adhesion and the visceral endoderm following ablation of nonmuscle myosin heavy chain II-A in mice. J Biol Chem 279:41263-41266.

31. Giannone, G., B. J. Dubin-Thaler, H. G. Dobereiner, N. Kieffer, A. R. Bresnick, and M. P. Sheetz. 2004. Periodic lamellipodial contractions correlate with rearward actin waves. Cell 116:431-443.

32. Dubin-Thaler, B. J., G. Giannone, H. G. Dobereiner, and M. P. Sheetz. 2004. Nanometer analysis of cell spreading on matrix-coated surfaces reveals two distinct cell states and STEPs. Biophys J 86:1794-1806.

33. du Roure, O., A. Saez, A. Buguin, R. H. Austin, P. Chavrier, P. Silberzan, and B. Ladoux. 2005. Force mapping in epithelial cell migration. Proc Natl Acad Sci U S A 102:2390-2395.

34. Döbereiner, H.-G., B. Dubin-Thaler, J. Hofman, H. Xenias, T. Sims, G. Giannone, M. L. Dustin, C. Wiggins, and M. P. Sheetz. 2006. Lateral Membrane Waves Constitute a Universal Dynamic Pattern of Motile Cells. Phys Rev Lett 97:038102.

35. Hastie, T., R. J. Tibshirani, and J. H. Friedman. 2001. The Elements of Statistical Learning Theory. Springer, New York, NY

36. Kittler, J. and J. Illingworth. 1986. Minimum error thresholding. Pattern Recognition 19:41-47.

37. Poggio, T., V. Torre, and C. Koch. 1985. Computational vision and regularization theory. Nature 317:314-319.

38. von Wichert, G., G. Jiang, A. Kostic, K. De Vos, J. Sap, and M. P. Sheetz. 2003. RPTP-alpha acts as a transducer of mechanical force on alphav/beta3-integrin-cytoskeleton linkages. J Cell Biol 161:143-153.

39. Burton, K., J. H. Park, and D. L. Taylor. 1999. Keratocytes generate traction forces in two phases. Mol Biol Cell 10:3745-3769.

40. Tan, J. L., J. Tien, D. M. Pirone, D. S. Gray, K. Bhadriraju, and C. S. Chen. 2003. Cells lying on a bed of microneedles: an approach to isolate mechanical force. Proc Natl Acad Sci U S A 100:1484-1489.

41. Chrzanowska-Wodnicka, M. and K. Burridge. 1996. Rho-stimulated contractility drives the formation of stress fibers and focal adhesions. J Cell Biol 133:1403-1415.

42. Helfman, D. M., E. T. Levy, C. Berthier, M. Shtutman, D. Riveline, I. Grosheva, A. Lachish-Zalait, M. Elbaum, and A. D. Bershadsky. 1999. Caldesmon inhibits nonmuscle cell contractility and interferes with the formation of focal adhesions. Mol Biol Cell 10:3097-3112.

43. Rottner, K., A. Hall, and J. V. Small. 1999. Interplay between Rac and Rho in the control of substrate contact dynamics. Curr Biol 9:640-648.

44. Pelham, R. J., Jr. and Y. Wang. 1997. Cell locomotion and focal adhesions are regulated by substrate flexibility. Proc Natl Acad Sci U S A 94:13661-13665.

45. Delanoe-Ayari, H., R. Al Kurdi, M. Vallade, D. Gulino-Debrac, and D. Riveline. 2004. Membrane and acto-myosin tension promote clustering of adhesion proteins. Proc Natl Acad Sci U S A 101:2229-2234.

46. Balaban, N. Q., U. S. Schwarz, D. Riveline, P. Goichberg, G. Tzur, I. Sabanay, D. Mahalu, S. Safran, A. Bershadsky, L. Addadi, and B. Geiger. 2001. Force and focal adhesion assembly: a close relationship studied using elastic micropatterned substrates. Nat Cell Biol 3:466-472.

47. Zaidel-Bar, R., C. Ballestrem, Z. Kam, and B. Geiger. 2003. Early molecular events in the assembly of matrix adhesions at the leading edge of migrating cells. J Cell Sci 116:4605-4613.

48. Riveline, D., E. Zamir, N. Q. Balaban, U. S. Schwarz, T. Ishizaki, S. Narumiya, Z. Kam, B. Geiger, and A. D. Bershadsky. 2001. Focal contacts as mechanosensors: externally applied local mechanical force induces growth of focal contacts by an mDia1-dependent and ROCK-independent mechanism. J Cell Biol 153:1175-1186.

49. Sawada, Y. and M. P. Sheetz. 2002. Force transduction by Triton cytoskeletons. J Cell Biol 156:609-615.

50. Jurado, C., J. R. Haserick, and J. Lee. 2005. Slipping or gripping? Fluorescent speckle microscopy in fish keratocytes reveals two different mechanisms for generating a retrograde flow of actin. Mol Biol Cell 16:507-518.

51. Henson, J. H., T. M. Svitkina, A. R. Burns, H. E. Hughes, K. J. MacPartland, R. Nazarian, and G. G. Borisy. 1999. Two components of actin-based retrograde flow in sea urchin coelomocytes. Mol Biol Cell 10:4075-4090.

52. Ponti, A., M. Machacek, S. L. Gupton, C. M. Waterman-Storer, and G. Danuser. 2004. Two distinct actin networks drive the protrusion of migrating cells. Science 305:1782-1786.

53. Kelley, C. A., J. R. Sellers, D. L. Gard, D. Bui, R. S. Adelstein, and I. C. Baines. 1996. Xenopus nonmuscle myosin heavy chain isoforms have different subcellular localizations and enzymatic activities. J Cell Biol 134:675-687.

54. Kovacs, M., F. Wang, A. Hu, Y. Zhang, and J. R. Sellers. 2003. Functional divergence of human cytoplasmic myosin II: kinetic characterization of the non-muscle IIA isoform. J Biol Chem 278:38132-38140.

55. Uchida, K. S., T. Kitanishi-Yumura, and S. Yumura. 2003. Myosin II contributes to the posterior contraction and the anterior extension during the retraction phase in migrating Dictyostelium cells. J Cell Sci 116:51-60.

56. Wessels, D., D. R. Soll, D. Knecht, W. F. Loomis, A. De Lozanne, and J. Spudich. 1988. Cell motility and chemotaxis in Dictyostelium amebae lacking myosin heavy chain. Dev Biol 128:164-177.

57. Suter, D. M. and P. Forscher. 2000. Substrate-cytoskeletal coupling as a mechanism for the regulation of growth cone motility and guidance. J Neurobiol 44:97-113.

58. Suter, D. M., L. D. Errante, V. Belotserkovsky, and P. Forscher. 1998. The Ig superfamily cell adhesion molecule, apCAM, mediates growth cone steering by substrate-cytoskeletal coupling. J Cell Biol 141:227-240.

59. Dobereiner, H. G., B. J. Dubin-Thaler, G. Giannone, and M. P. Sheetz. 2005. Force sensing and generation in cell phases: analyses of complex functions. J Appl Physiol 98:1542-1546.

60. Medeiros, N. A., D. T. Burnette, and P. Forscher. 2006. Myosin II functions in actin-bundle turnover in neuronal growth cones. Nat Cell Biol 8:215-226.

61. Turney, S. G. and P. C. Bridgman. 2005. Laminin stimulates and guides axonal outgrowth via growth cone myosin II activity. Nat Neurosci 8:717-719.

62. Gomes, E. R., S. Jani, and G. G. Gundersen. 2005. Nuclear movement regulated by Cdc42, MRCK, myosin, and actin flow establishes MTOC polarization in migrating cells. Cell 121:451-463.

63. Togo, T. and R. A. Steinhardt. 2004. Nonmuscle myosin IIA and IIB have distinct functions in the exocytosis-dependent process of cell membrane repair. Mol Biol Cell 15:688-695.

64. Fukui, Y., T. Kitanishi-Yumura, and S. Yumura. 1999. Myosin II-independent F-actin flow contributes to cell locomotion in dictyostelium. J Cell Sci 112 (Pt 6):877-886.

Table 1 Micro-post assay of force-generation capacity of control cells and NMM-II-deficient cells

	Force/post (nN)	Total cell force (nN)	% Relative to control force
RPTP-control	0.23 ± 0.07 (n = 18)	378 ± 113 (n = 18)	100
RPTP-C6	0.12 ± 0.03 (n = 20)	202 ± 38 (n = 20)	53.4
NIH3T3-control	0.23 ± 0.05 (n = 18)	276 ± 78 (n = 18)	100
NIH3T3-C4	0.10 ± 0.03 (n = 20)	115 ± 31 (n = 20)	41.6
NMM-IIB$^{+/+}$	0.18 ± 0.04 (n = 18)	178 ± 29 (n = 18)	100
NMM-IIB$^{-/-}$	0.17 ± 0.06 (n = 24)	123 ± 38 (n = 24)	69.1
NMM-IIB$^{-/-}$_IIAKD	0.06 ± 0.02 (n = 26)	46 ± 21 (n = 26)	25.8
NMM-IIB$^{+/+}$ (LPA)	0.23 ± 0.03 (n = 17)	171 ± 30 (n = 17)	96.1
NMM-IIB$^{-/-}$ (LPA)	0.18 ± 0.04 (n = 18)	118 ± 34 (n = 18)	66.3
NMM-IIB$^{-/-}$_IIAKD (LPA)	0.07 ± 0.02 (n = 17)	53 ± 20 (n = 17)	29.8
NMM-IIB$^{+/+}$ (blebbistatin)	0.06 ± 0.02 (n = 19)	38 ± 20 (n = 19)	21.3
NMM-IIB$^{+/+}$ (CD)	0.03 ± 0.02 (n = 15)	21 ± 7.1 (n = 15)	11.8
RPTP-control (CD)	0.04 ± 0.02 (n = 14)	31 ± 8.0 (n = 14)	8.2
NIH3T3-control (CD)	0.04 ± 0.02 (n = 17)	28 ± 6.5 (n = 17)	10.1

Total cell force was obtained by multiplying the total post displacement by the spring constant. The average force/post was calculated by dividing the total cell force by the number of micro-posts covered by a cell. Systematic error (~0.0155 nN per post) was excluded in the calculation of force/post and total cell force. Force values shown are average ± standard deviation. LPA: lysophosphatidic acid. CD: cytochalasin D.

FIGURE LEGENDS

FIGURE 1 Force generation involves NMM-IIA. (*A*) Cell lysates from six cell lines were subjected to Western blotting for NMM-IIA, NMM-IIB, vinculin, and β-actin. The RPTP-C6 and NIH3T3-C4 cells containing the NMM-IIA siRNA expression plasmid have lower expression levels of NMM-IIA than their respective control cells. RPTP-control-1 and NIH3T3-control-1 were untransfected control cells. RPTP-control-2 (designated as RPTP-control in other experiments) and NIH3T3-control-2 (designated as NIH3T3-control in other experiments) were cells transfected with a control siRNA plasmid. (*B*) A representative bright-field image of living cells spreading on arrays of 10 μg/ml fibronectin-coated micro-posts (1 μm in diameter and 2 μm center-to-center) in the presence of serum for 90 min at 37°C. Each bright spot represents the tip of a post. Posts covered by the cell are within the green circles automatically generated by a custom multiple-particle tracking program (See Meterials and Methods for details). Cells pulled posts inward along the cell edge. Scale bar, 10 μm. Inset is a higher magnification view of posts boxed in the red square. (*D*) Western blot analysis of lysates of NMM-IIB$^{-/-}$_IIAKD and NMM-IIB$^{-/-}$ cells (with control plasmid), showing that NMM-IIA expression is suppressed in NMM-IIB$^{-/-}$_IIAKD cells.

FIGURE 2 NMM-IIA is essential for focal adhesion and stress fiber formation. Control cells and NMM-IIA-knockdown cells were spread on coverslips coated with 10 μg/ml fibronectin for 90 min at 37°C, and then fixed and subjected to immunostaining. RPTP-control, RPTP-C6, NIH3T3-control, and NIH3T3-C4 cells were triple stained for NMM-IIA, F-actin, and vinculin. NMM-IIA was visualized with polyclonal antibody and Alexa 647-conjugated secondary antibody; F-actin was visualized with Alexa 568-phalloidin; vinculin was visualized with monoclonal antibody and Alexa 488-conjugated secondary antibody. NMM-IIA and F-actin images are epifluorescence; vinculin images are TIRF. Focal adhesion maps were generated using ImageJ software. Vinculin acts as an indicator of focal adhesions. Scale bars, 10 μm.

FIGURE 3 Quantitative comparisons of the focal adhesions in control and NMM-IIA-knockdown cells. On fibronectin substrate, the area of focal adhesions in NMM-IIA-deficient cells is significantly smaller than controls. The focal adhesion area in RPTP-C6 cells (82.0 ± 19.4 μm^2) is ~34% of that of RPTP-control cells (243.3 ± 50.4 μm^2). The focal adhesion area in NIH3T3-C4 cells (33.0 ± 6.4 μm^2) is ~25% of that of NIH3T3-control cells (133.8 ± 28.3 μm^2). Each measurement is from 16-20 cells. T-test, $P<0.005$. Error bars show standard deviation.

FIGURE 4 Retrograde F-actin flow is driven by NMM-IIA, not NMM-IIB. (*A*) A differential interference contrast image taken from a time-lapse movie of fibronectin-coated 2.7-μm magnetic beads transported on the surface of a MEF cell. White arrow depicts the centripetal direction of bead movement. The white line fragment in parallel to the white arrow spans a 3.0-μm-wide region used to analyze the velocity of bead movement. Scale bar, 5 μm. (*B*) Representative beads transported on control MEF cells (RPTP-control) and NMM-IIA-knockdown MEF cells (RPTP-C6) cells were sampled, and the distance from the center of the beads to the leading edge of the cell was plotted *versus* time. The fragments of the traces between the two horizontal lines (3.0 μm apart, as indicated by the double-headed arrow) correspond to the travel distance of beads as depicted by the white line fragment in (*A*). (*C*) Average velocity of bead movement on RPTP-control cells and RPTP-C6 cells. T-test, $P<0.001$.

(*D*) Bead movement rate is similar on NMM-IIB$^{+/+}$ cells and NMM-IIB$^{-/-}$ cells. Average velocity of bead movement on NMM-IIB$^{-/-}$_IIAKD cells is significantly slower than on NMM-IIB$^{+/+}$ cells and NMM-IIB$^{-/-}$ cells (untransfected cells or cells transfected with control plasmid). T-test, P<0.001. Error bars show standard deviation.

FIGURE 5 NMM-IIA regulates cell spreading of mouse embryonic fibroblasts. (*A*) Sequential TIRF images of a Calcein AM-labeled MEF cell spreading on fibronectin substrate. *B*, *C*, and *D* are plots of cell area over a course of time. NMM-IIB$^{+/+}$ and NMM-IIB$^{-/-}$ cells spread to similar areas on fibronectin substrate at early times (within 16 min) (*B*); RPTP-C6 cells spread significantly faster than RPTP-control cells (*C*); NIH3T3-C4 cells spread significantly faster than NIH3T3-control cells (*D*). Error bars show standard deviation. (*E-H*) are velocity maps as given by plotting velocity of protrusion/retraction of points at cell edge as a function of time and arc length (length of entire cell edge) which were obtained by analyzing 10-second interval time-lapse TIRF images of Calcein-AM labeled cells spreading on fibronectin at 37 °C. Briefly, time-lapse image sequences were analyzed with Matlab to obtain a closed curve delineating the cell edge, which was then parameterized by arc length. For each point on the cell boundary in each frame of time-lapse sequential images, the normal velocity was calculated and displayed in color-coded plots. Points on the cell boundary are specified by time (in minutes) and arc length (in μm); red coloring represents protrusion events while blue represents retraction events as depicted by the velocity bars. Velocities with an absolute value less than 0.5 μm/min were not considered to be relevant events. They are reflected as colorless patches among red and blue patches. Details are described in Materials and Methods section. *E*, *F*, *G*, and *H* are representative samples of RPTP-control, RPTP-C6, NIH3T3-control, and NIH3T3-C4 cells, respectively.

FIGURE 6 The distributions and dynamics of NMM-IIA and NMM-IIB are different in spreading MEF cells. (*A*) TIRF images (60x) of GFP-NMM-IIA and GFP-NMM-IIB taken from 5-second interval time-lapse sequential images of spreading RPTP cells at 37°C. Cell contours are outlined in white. White lines perpendicular to the cell edge are examples of locations used to generate kymograph of GFP-NMM-IIA and GFP-NMM-IIB clusters. There are little or no NMM-IIs in lamellipodia. (*B*) Examples of kymograph analysis of clusters of GFP-NMM-IIA and GFP-NMM-IIB. The white lines in *B* emphasize the rearward movement rates of the NMM-II clusters. (*C*) Average rearward movement velocities of GFP-NMM-IIA and GFP-NMM-IIB clusters calculated from kymographs. T-test, P<0.001. Error bars show standard deviation. (*D*) Epifluorescence images (40x) of immunostained endogenous NMM-IIA and NMM-IIB in RPTP cells plated for ~15min. Scale bars, 5 μm.

A

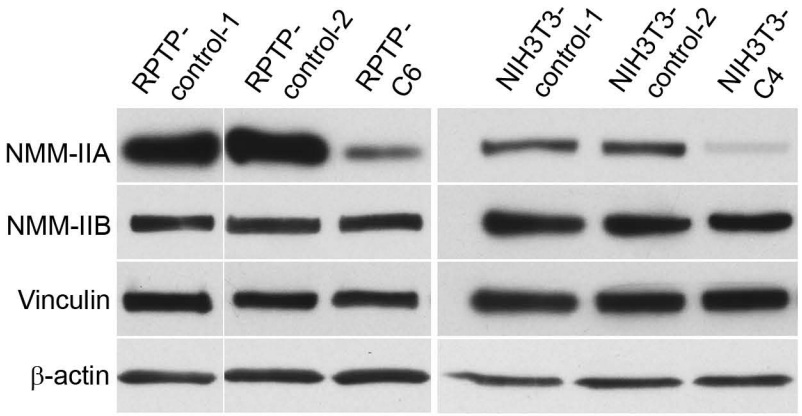

B

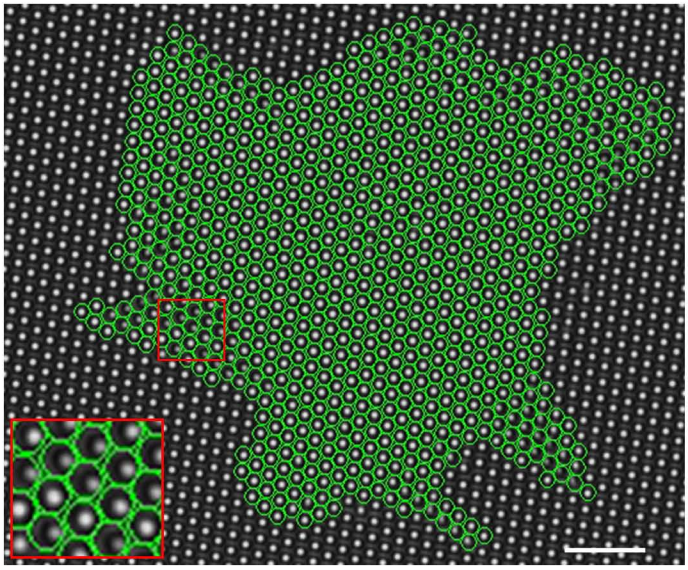

C

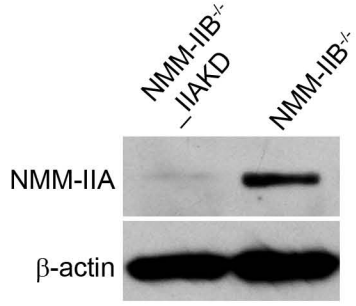

Cai_figure1

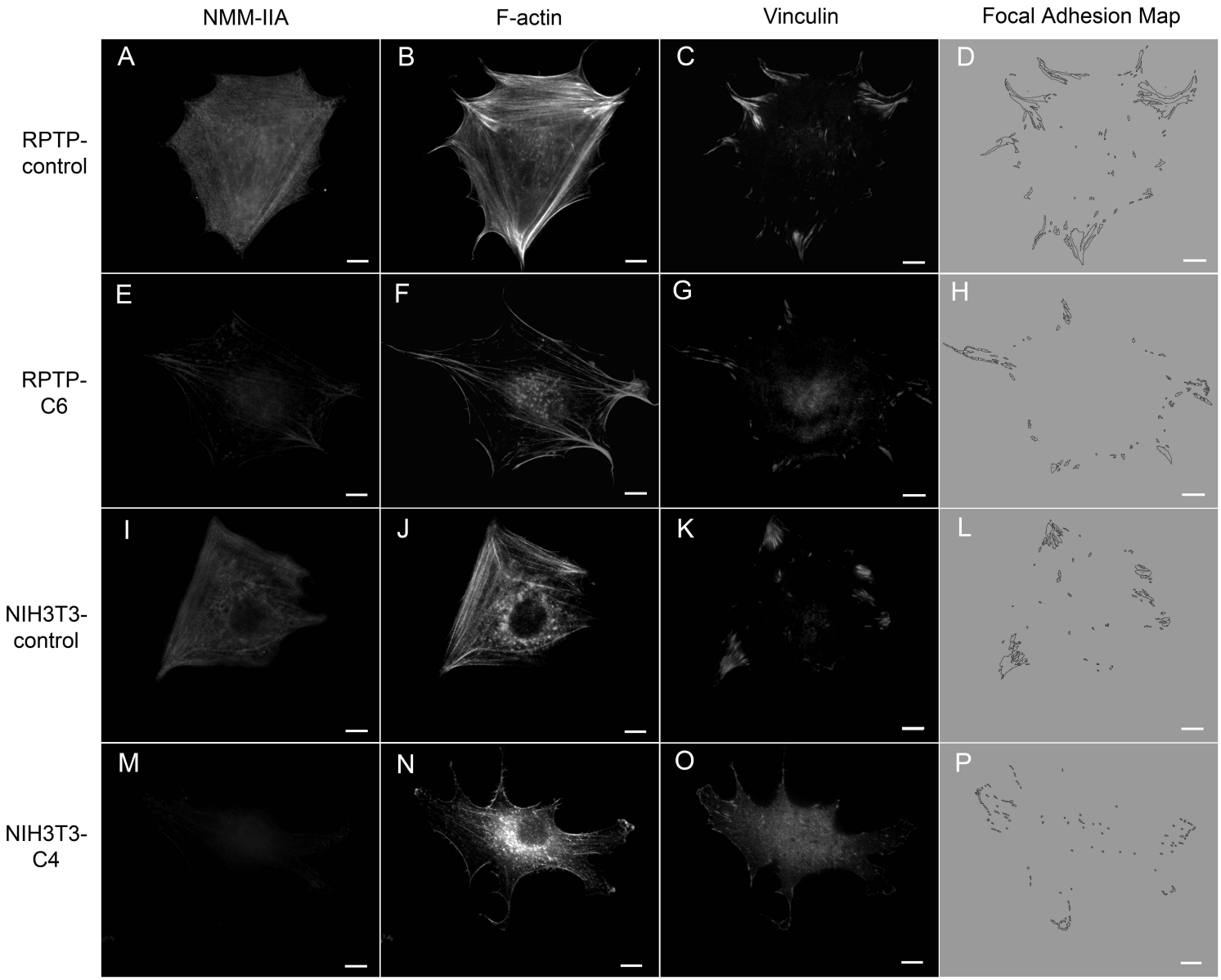
NMM-IIA
F-actin
Vinculin
Focal Adhesion Map
RPTP-control
RPTP-C6
NIH3T3-control
NIH3T3-C4
A
B
C
D
E
F
G
H
I
J
K
L
M
N
O
P

Cai_figure2

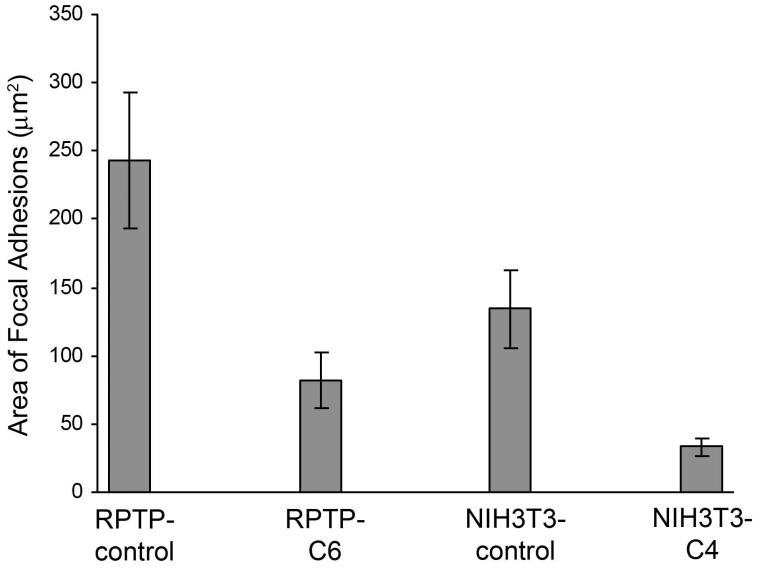
Area of Focal Adhesions (μm²)
350
300
250
200
150
100
50
0
RPTP-control
RPTP-C6
NIH3T3-control
NIH3T3-C4

Cai_figure3

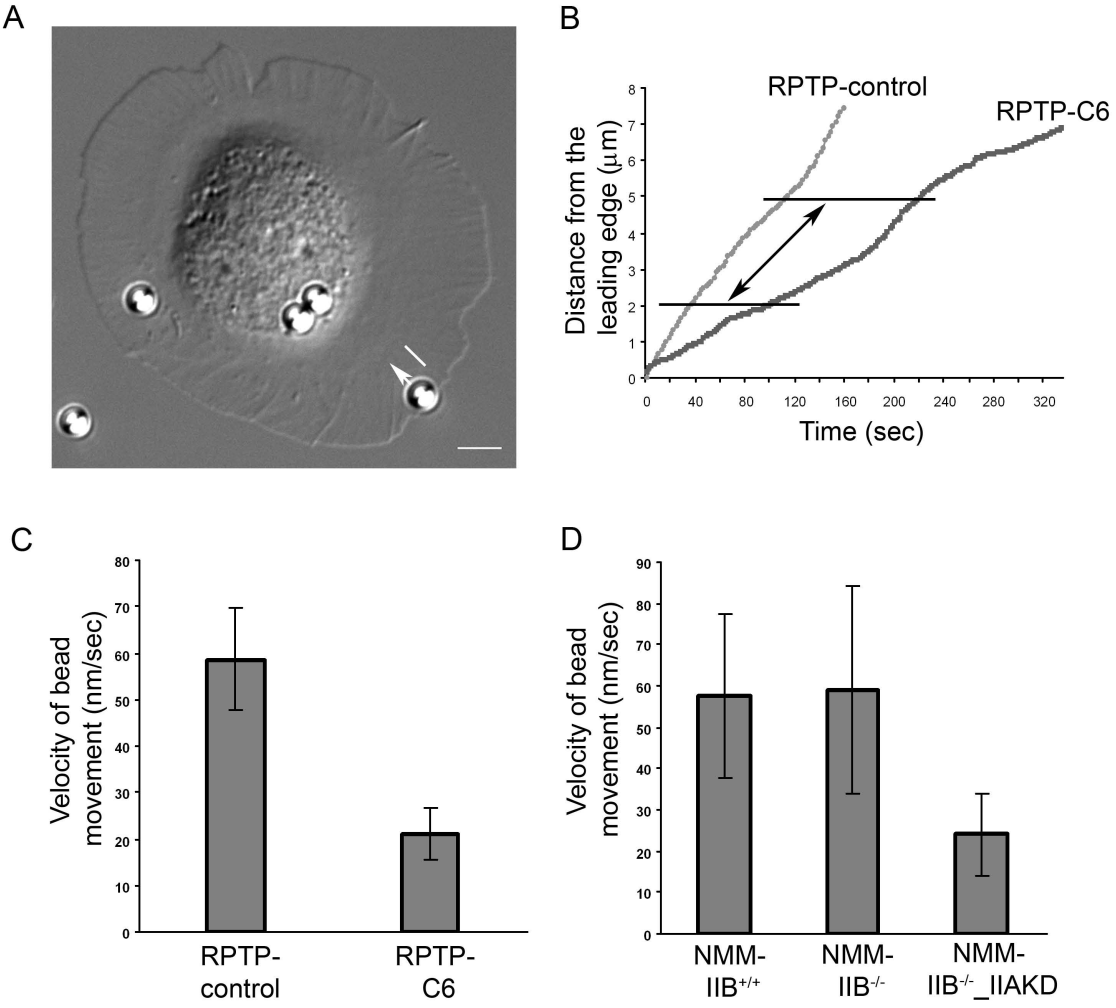
A
B
RPTP-control
RPTP-C6
Distance from the leading edge (μm)
Time (sec)
C
Velocity of bead movement (nm/sec)
RPTP-control
RPTP-C6
D
Velocity of bead movement (nm/sec)
NMM-IIB+/+
NMM-IIB-/-
NMM-IIB-/-_IIAKD

Cai_figure4

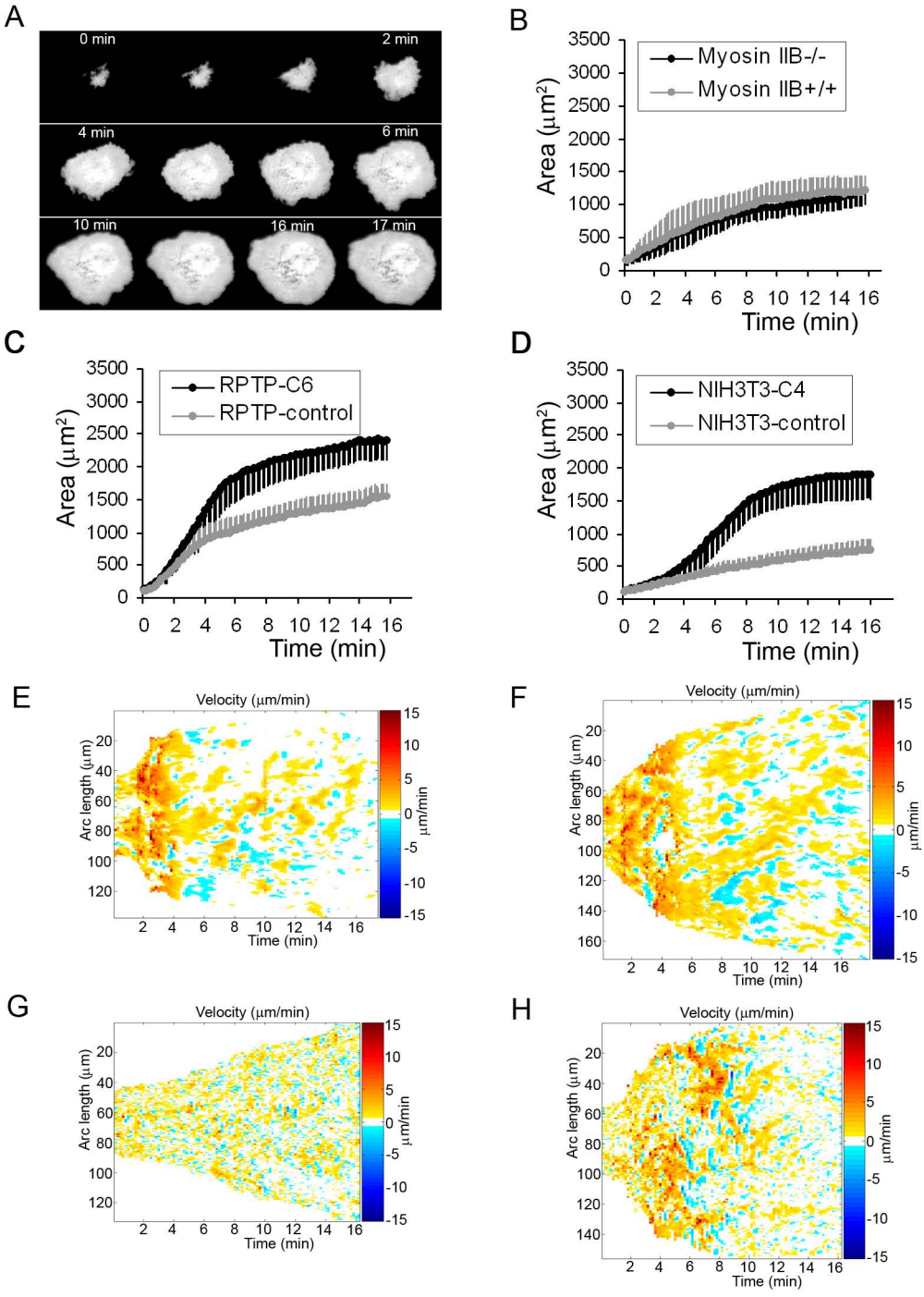
A
0 min
2 min
4 min
6 min
10 min
16 min
17 min
B
Myosin IIB-/-
Myosin IIB+/+
Area (μm²)
Time (min)
C
RPTP-C6
RPTP-control
Area (μm²)
Time (min)
D
NIH3T3-C4
NIH3T3-control
Area (μm²)
Time (min)
E
Velocity (μm/min)
Arc length (μm)
Time (min)
μm/min
F
Velocity (μm/min)
Arc length (μm)
Time (min)
μm/min
G
Velocity (μm/min)
Arc length (μm)
Time (min)
μm/min
H
Velocity (μm/min)
Arc length (μm)
Time (min)
μm/min

Cai_figure5

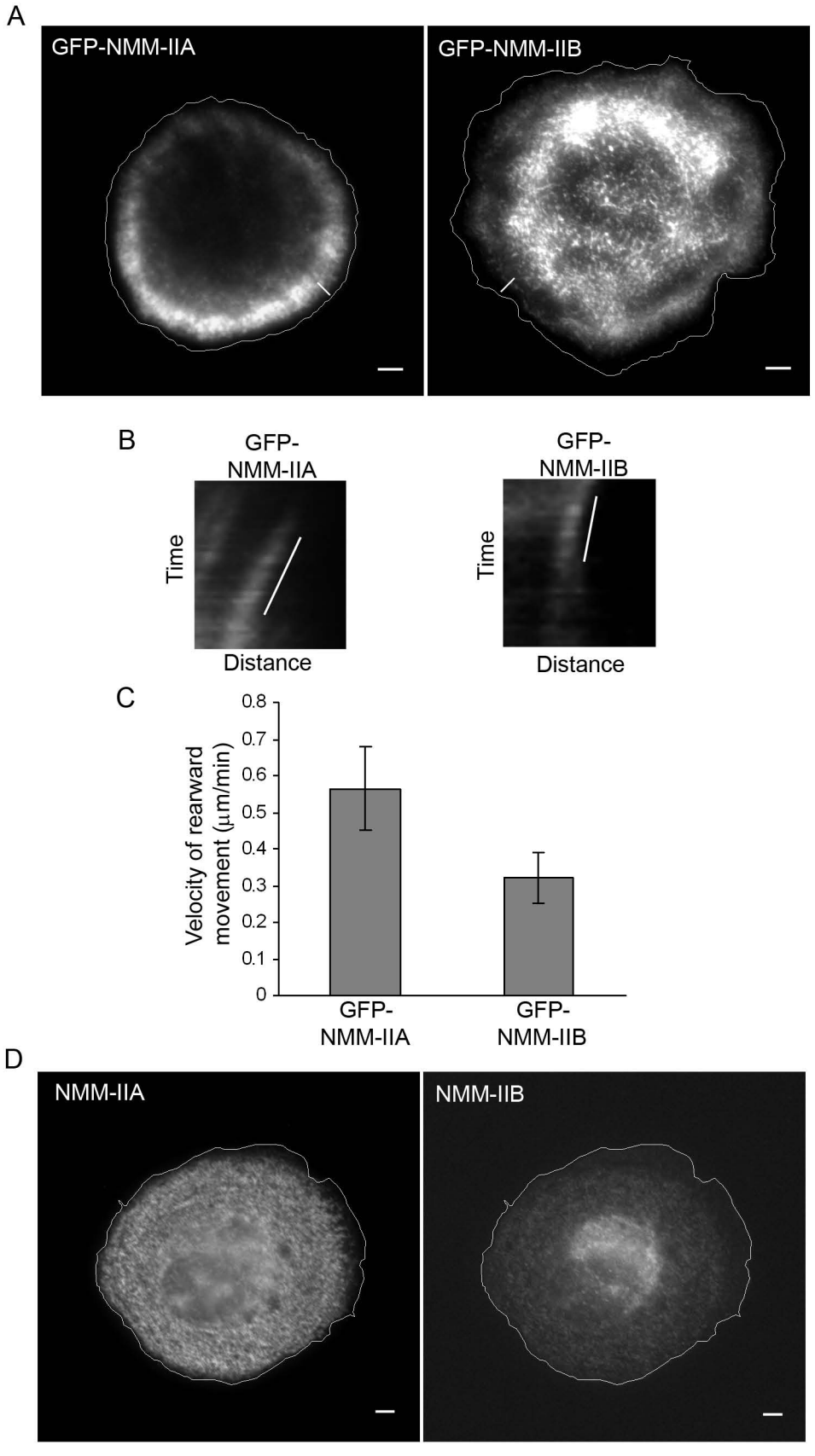
A
GFP-NMM-IIA
GFP-NMM-IIB
B
GFP-
NMM-IIA
GFP-
NMM-IIB
Time
Distance
Time
Distance
C
Velocity of rearward movement (μm/min)
0.8
0.7
0.6
0.5
0.4
0.3
0.2
0.1
0
GFP-
NMM-IIA
GFP-
NMM-IIB
D
NMM-IIA
NMM-IIB

Cai_figure6